Energy & Environmental Science

Cite this: *Energy Environ. Sci.*, 2012, **5**, 9618

www.rsc.org/ees

PAPER

Nitrogen doping of graphene and its effect on quantum capacitance, and a new insight on the enhanced capacitance of N-doped carbon†

Li Li Zhang,‡[a] Xin Zhao,‡[ab] Hengxing Ji,[a] Meryl D. Stoller,[a] Linfei Lai,[a] Shanthi Murali,[a] Stephen Mcdonnell,[c] Brandon Cleveger,[a] Robert M. Wallace[c] and Rodney S. Ruoff*[a]

Received 11th September 2012, Accepted 13th September 2012
DOI: 10.1039/c2ee23442d

Many researchers have used nitrogen (N) as a dopant and/or N-containing functional groups to enhance the capacitance of carbon electrodes of electrical double layer (EDL) capacitors. However, the physical mechanism(s) giving rise to the interfacial capacitance of the N-containing carbon electrodes is not well understood. Here, we show that the area-normalized capacitance of lightly N-doped activated graphene with similar porous structure increased from 6 μF cm^{-2} to 22 μF cm^{-2} with 0 at%, and 2.3 at% N-doping, respectively. The quantum capacitance of pristine single layer graphene and various N-doped graphene was measured and a trend of upwards shifts of the Dirac Point with increasing N concentration was observed. The increase in bulk capacitance with increasing N concentration, and the increase of the quantum capacitance in the N-doped monolayer graphene *versus* pristine monolayer graphene suggests that the increase in the EDL type of capacitance of many, if not all, N-doped carbon electrodes studied to date, is primarily due to the modification of the electronic structure of the graphene by the N dopant. It was further found that the quantum capacitance is closely related to the N dopant concentration and N-doping provides an effective way to increase the density of the states of monolayer graphene.

Introduction

The physical and chemical properties of carbon materials are critical to their performance as electrodes in supercapacitors.[1,2] A large electrochemically accessible surface area, appropriate pore size and distribution, good interconnectivity of pores, continuous pathways for rapid ion transport, large electrical conductivity, and good wettability are all important factors for the electrode material of an electrical double layer (EDL) capacitor. Though substantial effort has been devoted to increase the energy density, saturation of capacitance at lower than desirable levels is often observed in carbon-based electrodes,[3] especially for carbons with high surface

[a]*Department of Mechanical Engineering and the Materials Science and Engineering Program, The University of Texas at Austin, 1 University Station C2200, Austin, TX 78712, USA. E-mail: r.ruoff@mail.utexas.edu*
[b]*State Key Laboratory for Modification of Chemical Fibers and Polymer Materials, College of Materials Science and Engineering, Donghua University, Shanghai, 201620, P. R. China*
[c]*Department of Materials Science and Engineering, The University of Texas at Dallas, Richardson, Texas 75083, USA*

† Electronic supplementary information (ESI) available: EIS analysis, charge–discharge plots, the interfacial capacitance of the flat metal surface, experimental details and physical properties of aMEGOs. See DOI: 10.1039/c2ee23442d

‡ These authors contributed equally to this work.

Broader context

Many researchers have observed saturation of capacitance at lower than desired levels in high surface area carbon-based electrodes, especially for carbons with high surface areas and thin walls composed of what might be considered to be single or few layer graphene. Hence, a fundamental understanding of the underlying physical mechanisms that affect the interfacial capacitance of electrodes is of great interest, and also relevant if further increases in charge storage at the electrochemical interface between an electrode and an electrolyte are to be made. We found that the area-normalized capacitance of activated graphene and lightly N-doped activated graphene with similar porous structure increased from 6 μF cm^{-2} to 22 μF cm^{-2} for 0 at%, and 2.3 at% N-doping, respectively. The increase in bulk capacitance with increasing N concentration, and an increase in magnitude of quantum capacitance in N-doped monolayer graphene *versus* pristine monolayer graphene suggests that the increase in the electrochemical-double-layer type of capacitance of many, if not all, N-doped carbon electrodes studied to date is primarily due to the modification of the electronic structure of the graphene by the N dopant.

areas and thin walls composed of what might be considered to be single or few layer graphene (which however is not typically pristine graphene, but is rather chemically modified graphene).

Our previous study showed that for 'graphene' (reduced graphene oxide) material with a BET (Brunauer–Emmett–Teller) specific surface area (S_{BET}) of 705 m^2 g^{-1}, the surface area-normalized capacitance (with that S_{BET} value) was 19 μF cm^{-2} and 14 μF cm^{-2} for aqueous electrolyte and organic electrolyte, respectively;[4] but for the 3100 m^2 g^{-1} BET specific surface area 'activated microwave expanded graphite oxide' ('aMEGO') material consisting of atom-thick walls, the specific capacitance was only 6 μF cm^{-2} and 5 μF cm^{-2} under the same test conditions (again, using the S_{BET}).[5,6] (We appreciate that simply using the S_{BET} values to extract such area-normalized values may be an oversimplification, as we do not know the actual surface area that contacts the electrolyte, and the actual surface area accessed in the 'BET 705 m^2 g^{-1} material' may be higher.) Even considering the effect of micro-porosity, the area-normalized capacitance reported by Gogotsi and Simon's team was in the range of 8–13 μF cm^{-2} for their microporous carbide-derived carbon electrodes with average pore sizes from 0.6 to 2.25 nm.[7] This suggests that a factor other than porosity is playing a role in the interfacial capacitance in porous carbon materials having single or few-layer thick pore walls.

Some researchers have shown capacitance enhancement of carbon electrodes by substitutional doping with nitrogen and/or functionalization with N-containing groups.[8–17] However, the underlying physical mechanism(s) that gives rise to the interfacial capacitance of the N-containing carbon electrodes is not yet known.[13] Xia *et al.*, recently measured the quantum capacitance of graphene in an ionic liquid electrolyte and proposed that it might be the origin of the small interfacial capacitance observed in some carbon-based electrodes.[18] Our group has also begun to develop a fundamental understanding of interfacial capacitance of one side, and then also of both sides, of suspended monolayer graphene.[6] Our results showed that the area normalized charge that can be stored simultaneously on both sides is significantly lower than could be stored on just one side of monolayer graphene (due to quantum capacitance in pristine, monolayer graphene), suggesting that quantum capacitance[18–21] could be a limiting factor for the interfacial capacitance of certain highly porous carbon electrode materials. In this study, we show that the area-normalized capacitance of lightly N-doped activated graphene with similar porous structure increased from 6 μF cm^{-2} to 22 μF cm^{-2} with 0 at%, and 2.3 at% N-doping, respectively. The increase in bulk capacitance with increasing N concentration, and the increase of the quantum capacitance in the N-doped monolayer graphene *versus* pristine monolayer graphene suggests that the increase in the EDL type of capacitance of many, if not all, N-doped carbon electrodes studied to date, is primarily due to the modification of the electronic structure of the graphene by the N dopant.

Experimental

Synthesis of aMEGO and N-doped aMEGOs

The synthesis of aMEGO was carried out as described in ref. 5. Briefly, microwave exfoliated graphite oxide (MEGO), prepared from graphite oxide (GO) by microwave exfoliation was dispersed and soaked in aqueous KOH for 20 hours. The solid cake obtained after filtration of excess KOH was dried. The activation temperature was maintained at 700 °C and 800 °C as described in ref. 5 for aMEGO700 and aMEGO800, respectively, for 1 hour in a horizontal tube furnace (50 mm diameter), with an argon flow of 120 sccm at a pressure of one atmosphere. N-doped aMEGOs were prepared similarly to that of aMEGO, with additional flow of ammonia gas during the activation process. The amount of nitrogen doping was controlled by varying the flow rate of ammonia gas to be 20, 30, and 40 sccm for N-doped aMEGO with 0.7 at%, 1.0 at% and 2.3 at%, respectively. The sample was allowed to cool down over a period of several hours, removed from the furnace and repeatedly washed with de-ionized water until a pH value of 7 was reached. The final materials were obtained after drying at 80 °C in ambient for 24 hours.

Synthesis of monolayer graphene and N-doped graphene

Cu foil (99.8%, Alfa-Aesar, item no. 13382) was cut into, typically, 2 cm × 10 cm strips and loaded at the center of a hot wall tube furnace consisting of a 22 mm diameter fused quartz tube heated in a split furnace (TF55035A-1, Linderburg/Blue M). The tube was evacuated, and then filled with 2 sccm hydrogen (99.999%, Airgas). The furnace was ramped to 1035 °C under flowing hydrogen at a pressure of 20 mTorr. The Cu foil was then annealed for 30 minutes before introducing carbon precursors. Methane (99.999%, Airgas) and pyridine (>99.0%, Aldrich) mixture at different partial pressure ratios were introduced at 1035 °C for 7 minutes in order to obtain graphene with different nitrogen doping levels. The total pressure for graphene growth was maintained at 70 mTorr as shown in Table S1.† The furnace was cooled down to room temperature at a rate varied between 20 and >100 °C per minute which resulted in graphene with no discernable difference from the pristine graphene grown without pyridine.

General characterization

The pore structure of the sample was investigated using physical adsorption of nitrogen at the liquid-nitrogen temperature (77 K) on an automatic volumetric sorption analyzer (NOVA2000, Quantachrome). Prior to measurement, each sample was vacuum-degassed at room temperature for 5 h. The specific surface area (S_{BET}) was determined according to the Brunauer–Emmett–Teller method in the relative pressure range of 0.05–0.2. Scanning electron microscopy (SEM) was conducted at 30 kV accelerating voltage (Quanta 600 FEG, FEI Company). X-ray photoelectron spectra (XPS) were collected using a monochromatic Al K X-ray source and Omicron EA125 hemispherical analyzer. The spectrometer was configured with an acceptance angle of ±8°, a takeoff angle of 45° and a 15 eV analyzer pass energy, operated in the constant analyzer energy (CAE) mode. The Raman spectra of graphene on SiO_2 were measured by a WITEC Alpha300 system with a 532 nm laser excitation source.

Supercapacitor measurements

Both three-electrode and two-electrode cell configurations were used to measure the performance of N-doped aMEGO and

un-doped aMEGO as a supercapacitor electrode. For a three-electrode cell setup, the slurry containing polytetrafluoroethylene (PTFE, Aldrich; 60 wt% dispersion in water) and aMEGO (aMEGO : PTFE = 95 : 5 in weight) was pressed onto a nickel foam (1 cm × 1 cm) and dried at 100 °C under vacuum to use as the working electrode. The three-electrode cell consisted of a Pt sheet and saturated calomel electrode as the counter and reference electrodes, respectively.

For a two-electrode cell configuration, PTFE was added to the aMEGO powder (aMEGO : PTFE = 95 : 5 in weight) as a binder. The aMEGO powder was mixed into a paste using a mortar and pestle, rolled into sheets of uniform thickness ranging from 30 to 50 μm thick (from sheet to sheet) and punched into 0.5 inch diameter electrodes after drying at 100 °C under vacuum. Two nearly identical (by weight and size) electrodes were assembled in a test cell consisting of two current collectors, two electrodes, and an ion-porous separator (Celgard® 3501) supported in a test fixture consisting of two stainless steel plates. 1 M $TEABF_4$ in AN, and 6 M KOH, solutions were used as the electrolytes in separate experiments.

Gravimetric capacitance for a single electrode was calculated from the discharge curve in a two-electrode cell as

$$C_{\text{single}} = \frac{4I\Delta t}{m\Delta V}$$

where I is the constant current and m is the total mass for both carbon electrodes, Δt is the discharge time and ΔV is the voltage change during the discharge process.

Gravimetric capacitance in a three-electrode cell was obtained as

$$C_{\text{single}} = \frac{I\Delta t}{m_s\Delta V}$$

where I is the constant current and m_s is the mass of the working electrode, Δt is the discharge time and ΔV is the voltage change during the discharge process.

The surface area normalized capacitance C_{SA} (μF cm^{-2}) was estimated from:

$$C_{SA} = \frac{C_{\text{single}}}{S_{BET}} \times 100$$

where S_{BET} is the specific surface area (m^2 g^{-1}) derived from the N_2 adsorption and C_{single} is the gravimetric capacitance in F g^{-1}.

The interfacial capacitance (C_T) of the PG and NG samples was measured in a three-electrode cell using an Eco Chemie Autolab PGSTAT100 Potentiostat equipped with the FRA2 frequency response analyzer module and Nova 1.5 software. Cyclic voltammograms were performed to detect any non-EDL behavior of the electrodes that would indicate the presence of impurities or faradic activity. Non-EDL behavior was not detected. The interfacial capacitance was determined using electrical impedance spectroscopy (EIS) with a sinusoidal signal with an amplitude of 10 mV over a frequency range of 100 kHz to 1 Hz. The capacitance values at each potential were determined by fitting the EIS spectra to an R(RC) equivalent circuit using Nova 1.5 software (Eco Chemie) with error less than 1%. The area-normalized capacitance is the capacitance divided by the graphene surface area exposed to the electrolyte.

Results and discussion

In an attempt to gain a deeper scientific understanding of the interfacial capacitance of N-containing carbon electrode materials, we prepared several lightly N-doped aMEGO materials with atom-thick walls and similar porous structures (*i.e.*, similar specific surface area, and pore size and pore size distribution). Fig. 1A shows the nitrogen adsorption/desorption isotherms of various aMEGO materials. The pore size and distribution of the N-doped aMEGOs are compared with pure aMEGOs, all activated using KOH at the same temperatures. The parameters describing porosity of these aMEGOs are listed in Table S2;† the N-doped aMEGO has a very similar isotherm and pore size distribution as that of the pure aMEGO. By maintaining essentially the same porous structure for all samples, any variance in capacitance can be attributed to the dopant. During the activation process, the N atoms replace carbon atoms in the aMEGO. X-ray photoelectron spectroscopy (XPS) analysis (Fig. 1B) confirmed the presence of N and two types of N dopants were identified, pyridinic N (N6) and pyrrolic N (N5), respectively.[22]

The effect of N dopants on capacitance was evaluated by conducting cyclic voltammetry (CV) and galvanostatic charge/discharge using a three-electrode electrochemical cell in 6 M KOH electrolyte with Pt sheet and saturated calomel electrode (SCE) as the counter and reference electrodes, respectively. At a scan rate of 20 mV s^{-1}, a cell with an N-doped aMEGO electrode (with 1.0 at% N) had much larger current than an electrode of pure aMEGO (Fig. 2A), indicating a greatly increased capacitance due to the N doping. The rate dependant gravimetric capacitance for various aMEGO electrodes that were activated at 700 °C with three N dopant concentrations are shown in Fig. 2B; the gravimetric capacitance increases with increase of N dopant concentration with the highest gravimetric capacitance obtained being about 420 F g^{-1}. In addition, with lightly doped N, the electrical conductivity of the aMEGO electrodes did not significantly decrease, as indicated by the small increase of the equivalent series resistance (ESR) from the electrochemical impedance analysis (Fig. S1†). The ESR for the N-doped aMEGO with N dopant concentration of 2.3 at% increased only about 0.5 ohms compared to that of the pure aMEGO electrode. More importantly, at a current density of 0.2 A g^{-1}, the area normalized capacitance increased from 6 μF cm^{-2} to 11 μF cm^{-2} and then to 22 μF cm^{-2} for N-doping levels of 0, 1.0 at%, and 2.3 at%, respectively (Fig. 2C). Similar capacitance enhancement was seen on N-doped aMEGO that was produced at 800 °C (Fig. 2D). Since the micro-porosity is similar in these carbon materials, the main parameter affecting the specific capacitance is the extent and type of N doping. To further test the effect of N doping, a two-electrode symmetrical supercapacitor cell was constructed using N-doped aMEGO as the electrodes and an aprotic electrolyte, 1 M $TEABF_4$ in acetonitrile (AN); aqueous KOH (6 M) electrolyte was also used in separate measurements. The two electrode cell yielded similar capacitance enhancements for N-doped aMEGO electrodes when tested in aqueous and aprotic electrolytes (Fig. 2D and S2†). These results prompted us try to understand the mechanism(s) for the increase in capacitance by N doping of aMEGO.

The values of interfacial capacitance of monolayer graphene and monolayer N-doped graphene might help in understanding

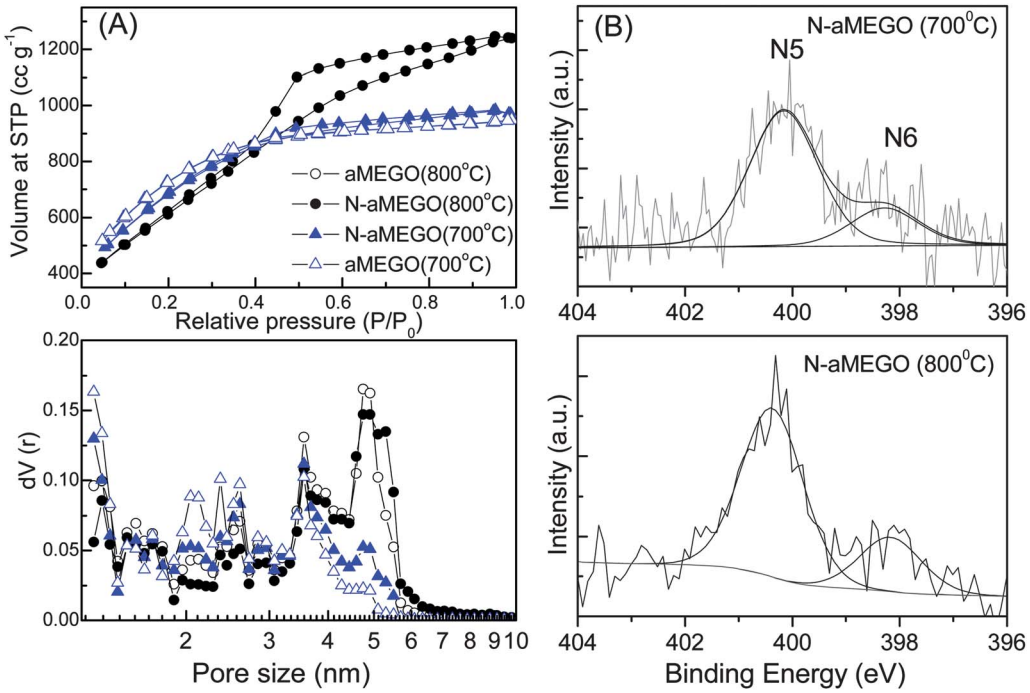

Fig. 1 (A) Nitrogen adsorption/desorption isotherms and pore size distribution for various aMEGO electrodes. (B) XPS N 1s spectrum of the N-doped aMEGO at different activation temperatures. Each N 1s peak is deconvoluted into two sub-peaks that correspond to pyridinic N (N-6) and pyrrolic N (N-5) bonding configurations.

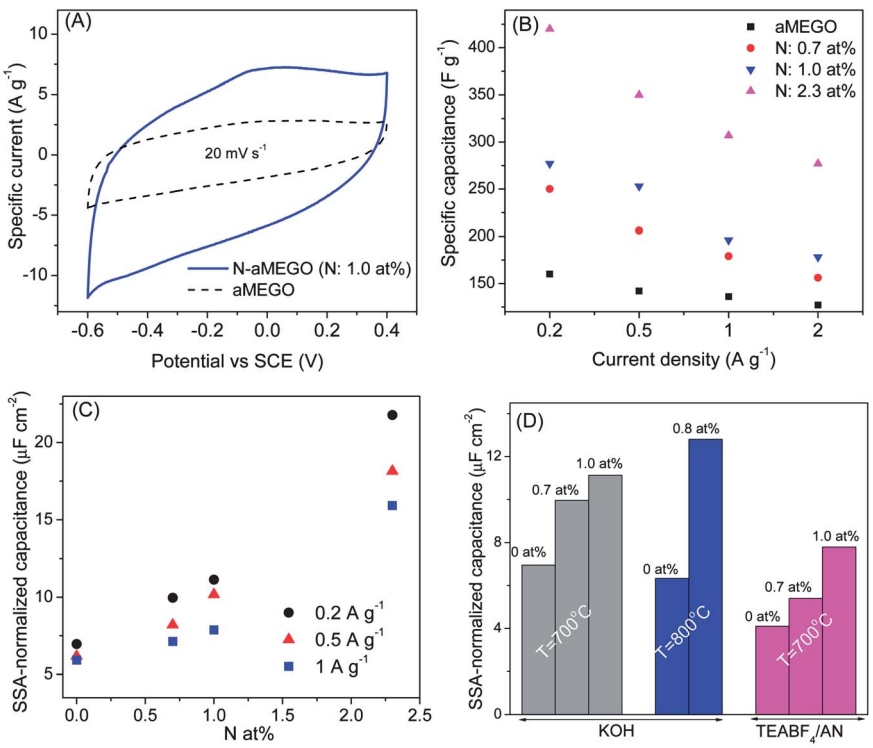

Fig. 2 Electrochemical performance of N–aMEGO based electrodes. (A) Cyclic voltammetry curves of aMEGO and N-doped aMEGO (with 1.0 at% of N and activation temperature of 700 °C) at a scan rate of 20 mV s^{-1}. (B) Gravimetric capacitance of various N-doped aMEGO electrodes in comparison to pure aMEGO measured at different current densities. The legend indicates various N–aMEGO samples with different N concentrations. (C) Specific surface-area (SSA) normalized capacitance as a function of N concentration at various current densities. (D) The SSA-normalized capacitance at various N concentrations for samples tested in both 6 M KOH electrolyte using a three-electrode setup and 1 M TEA BF_4/AN using a two-electrode cell configuration.

the mechanism(s) of the improved capacitance in N-doped aMEGO, given that the walls of the pores in the latter are atom-thick, like monolayer graphene. Pristine monolayer graphene and N-doped monolayer graphene were prepared by chemical vapor deposition on copper foils.[23,24] Raman spectroscopy can be used to identify the number of layers, structure, doping, and impurity levels as well as the 'quality' of graphene,[25–30] and Raman spectra are shown in Fig. 3 for pristine graphene (PG) and N-doped graphene (NG) that were transferred onto SiO_2 substrates. Fig. 3A shows maps of the G peak over a large area for PG and NG, respectively. The optical microscope image of the NG sample in Fig. 3B indicates a clean surface. The presence of the N dopants in the NG sample is confirmed by analysis of XPS data (Fig. 3C). Two types of N dopants were observed in the NG samples and they have the same bonding configurations as are present in the N-doped aMEGO samples (pyridinic N (N6) and pyrrolic N (N5)). Thus the N doping in NG resembles the N-doping in aMEGO. The histograms of the G peak positions for the pristine and N-doped graphene samples are shown in Fig. 3D. There is a clear shift in the position of the G peak for N-doped graphene, indicating the charge carrier concentration is significantly altered by the N doping.[29,31] The charge carrier concentration based on the shift in the position of the G peak in the Raman spectrum is estimated to be 1.1×10^{13} cm^{-2} for the NG sample,[29] which is much higher than the intrinsic electron and hole sheet densities in pristine graphene ($\sim 9 \times 10^{10}$ cm^{-2}).[32] The ratio of the 2D/G peak intensity was shown to be sensitive to dopant, charge carrier, and defect concentration.[29,31] Fig. 3E shows the Raman 2D/G peak intensity ratio mapping for PG and NG measured in the same area as that shown in Fig. 3A. The Raman spectra measured at different positions of PG (Fig. 3F) showed typical features of monolayer graphene: I_G/I_{2D} of $\sim$0.5 and a symmetric 2D band centered at $\sim$2680 cm^{-1} with a full width at half-maximum of $\sim$33 cm^{-1}.[23] Little or no signal at the D band was observed, indicating a low defect density. In contrast, the NG sample has a large D peak (Fig. 3G) as well as changes in the intensity of the G and 2D bands in the dark regions of the 2D/G map as seen from the Raman spectra recorded in the regions indicated by (II) and (III) in Fig. 3E; in the bright region marked by (I), the Raman spectrum has features similar to that of pristine graphene. The Raman spectra of NG were consistent with the presence of dopants or defects while preserving the basic structural properties of the graphene sheet. In addition, the 2D/G maps showed relatively uniform N doping over the entire mapping area.

The interfacial capacitance of relatively residue-free N-doped and pristine graphene was obtained as follows. The experimental setup is shown in Fig. 4A. A three-electrode cell was used with Pt wire and Ag/AgCl as the counter and reference electrodes, respectively. A high concentration aqueous electrolyte (6 M KOH) was used to minimize the effect of the diffuse-layer capacitance.[1] The graphene working electrode was formed by covering one side of the CVD grown graphene on a Cu foil substrate first with thin PMMA and then with insulating tape. The Cu substrate was then removed from the graphene in a bath of ammonium persulfate (0.5 M). A small portion of the Cu at the edges of the sample that is not immersed into the ammonium persulfate solution is protected from the etching and

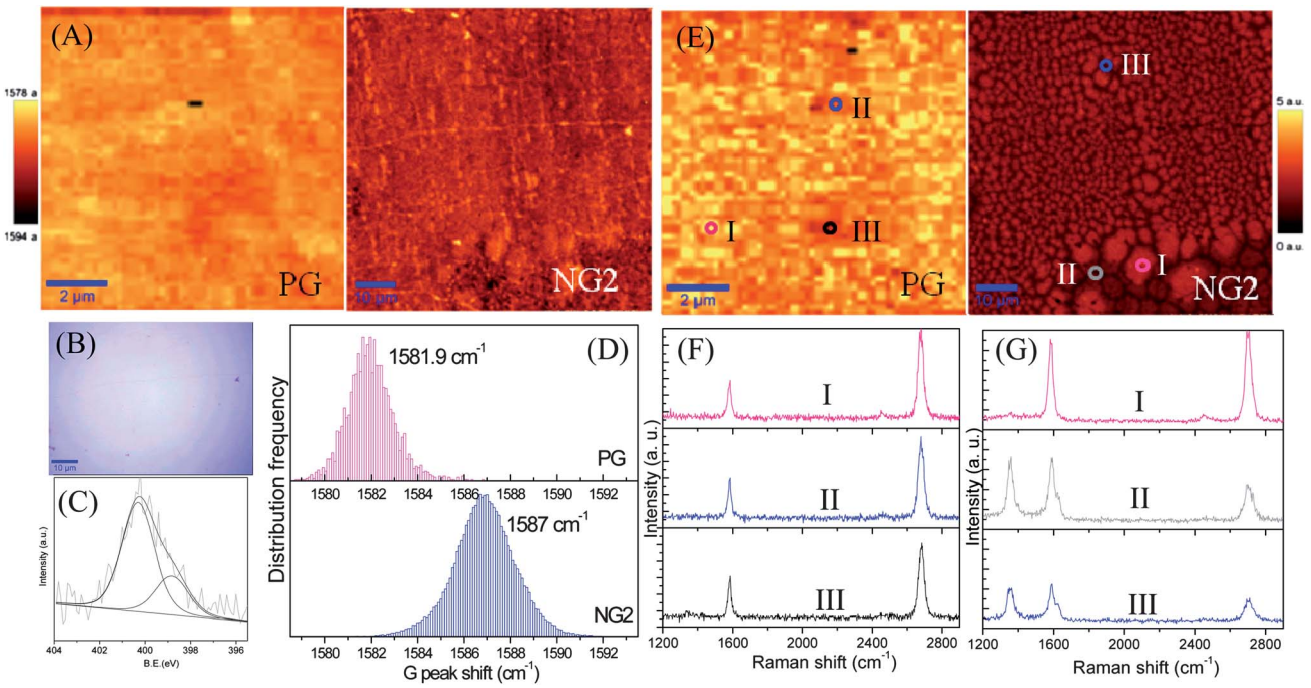

Fig. 3 Micro-Raman characteristics of pristine and N-doped graphene. (A) Maps of G peak position for pristine graphene (PG) and N-doped graphene (NG2) after transferring to a SiO_2/Si substrate. (B) Optical microscope image and (C) XPS N 1s spectrum of NG2. (D) Histogram of the G peak positions of PG and NG2 from the maps in (A). (E) Raman mapping of the ratio of the 2D/G peak intensities for PG and NG2 at the same position as shown in (A). (F and G) Raman spectra taken at different positions in (E) for NG and PG, respectively.

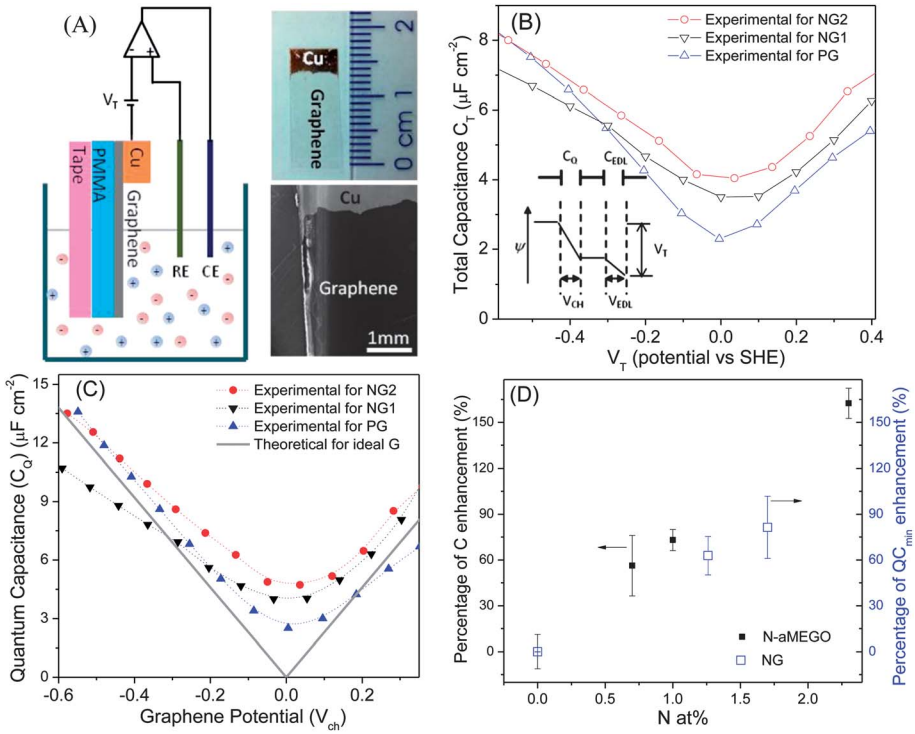

Fig. 4 (A) Scheme showing the quantum capacitance measurement setup. Photograph (right top) shows the dimension of the working electrode, where graphene with the un-dissolved portion of Cu foil as the electrode contact is on top of the PMMA and protected by the tape. The SEM image (bottom right) clearly shows the good contact between the graphene and Cu. (B) Total capacitance (C_T) obtained as a function of the total gate potential V_T. (C) Dependence of quantum capacitance (C_Q) on N dopant concentration as a function of graphene potential (V_{ch}). Experimentally measured C_Q of PG and the different NGs (solid symbols with dashed lines) in comparison to the theoretical curve of ideal G. (D) The correlation between the bulk capacitance obtained from the N–aMEGO based electrodes and the quantum capacitance from NGs as a function of N concentration. An increase for the bulk capacitance and quantum capacitance as a function of increasing N dopant concentration of the graphene is observed.

serves as the metal contact. This procedure eliminates the need to use the more conventional graphene transfer process and leaves the graphene electrode relatively free of residue. This is very important as the residual PMMA residue is essentially unavoidable during the normal graphene transfer (onto a SiO_2/Si substrate) process. Since both the interfacial capacitance and quantum capacitance are very sensitive to various impurities,[18,32,33] various residues on the graphene would cause secondary-doping (with the substitutional N contributing the primary doping).

Fig. 4B shows the measured total interfacial capacitance (C_T) as a function of the total gate potential (V_T) and Fig. 4C shows the quantum capacitance (C_Q) of various N-doped graphene and pristine graphene samples as a function of the graphene potential (V_{ch}), respectively. The theoretically predicted C_Q for ideal graphene is shown as a solid gray line in Fig. 4C for comparison. The quantum capacitance arises from the kinetic, exchange–correlation, and electron–phonon interaction energies in the total-energy function.[34] The kinetic term $\kappa_b T \ll eV_{ch}$, then C_Q can be expressed as:[32]

$$C_Q \cong e^2 \frac{2}{\pi} \frac{eV_{ch}}{(\hbar v_F)^2}, \text{ or } C_Q = e^2\,\mathrm{DOS}(eV_{ch})_{2D}$$

where v_F is the Fermi velocity of the Dirac electron, V_{ch} is the graphene potential and $\hbar$ is the Planck constant. $\mathrm{DOS}(eV_{ch})_{2D}$ is the linear density of states (DOS) of intrinsic carriers in the graphene sheet: $\mathrm{DOS}(eV_{ch})_{2D} = \frac{g_s g_v}{2\pi(\hbar v_F)^2}|eV_{ch}|$, where $g_s = 2$ for twofold spin degenerate and $g_v = 2$ (two valleys K and K' in the first Brillouin zone).

From the above expression, it can be seen that the quantum capacitance is closely related to the DOS, and increases linearly with V_{ch} with a slope of about 23 μF cm^{-1} V^{-1}. The measured interfacial capacitance of graphene can be considered as the result of the capacitance due to the EDL formed at the graphene–electrolyte interface connected in series with the quantum capacitance of graphene (Fig. 4B inset). The capacitance from the diffuse layer (C_{diff}) in the electrolyte can be neglected since highly concentrated electrolyte was used ($C_{diff} \gg C_{EDL}$). The C_{EDL} in 6 M KOH electrolyte on a flat Pt surface was measured to be 28 μF cm^{-2} (Fig. S3†), similar to previous reports.[6] Since both the interfacial capacitance and graphene potential depends on V_T, the following equations can be used to describe the system:

$$\frac{1}{C_T} = \frac{1}{C_Q} + \frac{1}{C_{EDL}}$$

$$C_Q \partial V_{ch} = C_T \partial V_T = C_{EDL} \partial V_{EDL}$$

$$\partial V_T = \partial V_{ch} + \partial V_{EDL}$$

Hence, the graphene potential can be written as:

$$V_{ch} = V_T - \int_0^{V_T} \frac{C_T}{C_{EDL}} \partial V_T$$

The graphene potential (V_{ch}) dependant C_Q is therefore extracted from C_T and is plotted in Fig. 4C. The shape of the measured C_Q of PG (blue dashed line) is very similar to the theoretically predicted curve for ideal graphene (solid gray line). The slope is approximately 22 μF cm^{-1} V^{-1} on each side of the Dirac Point and decreases when approaching the Dirac Point. The C_Q minimum appears around $V_{ch} = 0$ V, with a value of 2.5 μF cm^{-2}, higher than the predicated value of 0.8 μF cm^{-2}. The theoretical prediction is based on the assumption of a perfectly uniform and clean graphene sample. Imperfections exist in the real graphene sample, such as various kinds of defects, impurities, electron and hole puddles as a result of potential fluctuations in graphene, and thus the local density of states at a given Fermi energy fluctuates.[35–37] On the other hand, the slopes of the C_Q curves decrease and the C_Q minimum shifts upwards for N-doped graphene samples over a wide potential range. The results also show that as N concentration increases, the minimum C_Q value increases. The distinct and significant deviation from the theoretical prediction of the intrinsic quantum capacitance is greater than what is expected by a microscopic model of quantum capacitance in graphene developed by Xu *et al.*, using the local potential fluctuation as a parameter.[38] It is known that N-doping changes the electronic structure of the graphene and alters the charge carrier density significantly.[31,39] Therefore, the dopant induced carrier density is much larger than the carrier fluctuations caused by the local potential fluctuation. The change in the shape of the C_Q curves of the N-doped graphene samples are consistent with that predicted by considering the charge carrier density as one variable.[18] Note that the carrier density that arises from the local channel electrostatic potential of graphene without considering the dopant induced carrier density can be expressed as $n_Q = \frac{C_Q V_{ch}}{e} = \pm\left(\frac{eV_{ch}}{\hbar V_F \sqrt{\pi}}\right)^2$. Thus C_Q is related to n_Q by:

$$C_Q = \frac{e^2}{\hbar V_F \sqrt{\pi}} \sqrt{n_Q}$$

Since N-doping donates additional mobile electrons to the graphene lattice (Zhao *et al.*[31] obtain on average ~0.42 ± 0.07 mobile carriers for each N dopant), the additional dopant-induced mobile carriers will modify the quantum capacitance expression that is shown above. Though there is a similarity between our experimentally measured C_Q of the NG samples and the numerically simulated C_Q by Xia's model[18] in which the quantum capacitance is related to $\sqrt{n}$, $C_Q \propto \sqrt{n}$, it does not fit well to our experimental observations. A more complete model describing the quantum capacitance based on basic physical parameters such as potential fluctuation, impurities, and dopant types, still needs to be developed. Our results strongly suggest that the quantum capacitance and its contribution to the interfacial capacitance are closely related to dopant concentration for monolayer graphene. Clearly, there is a correlation between the modified quantum capacitance in N-doped *versus* un-doped graphene, and the observed increase in capacitance of the N-doped aMEGO *versus* un-doped aMEGO as shown in Fig. 4D. Increasing the N dopant concentration leads to both an enhancement of the total capacitance of aMEGO, and to an upward shift of the interfacial capacitance and C_Q of NGs. These results strongly suggest that the EDL charge storage by the N-doped aMEGO electrodes studied here has a quantum capacitance component.

Besides the 'pseudocapacitance' effect of the N functionalities from proton transfer that many researchers have adopted as the only explanation for the change in interfacial capacitance for N-doped carbons when compared to the values of the pure C analogs, another factor, the quantum capacitance, may thus be relevant for some carbons having thin walls where the response of the charge inside the near 2-D walls may have to be considered.

Conclusions

In summary, we have investigated the effect of N doping on specific capacitance in both lightly N-doped aMEGO materials and monolayer graphene. The strong correlation between the increase in capacitance of the N-doped aMEGO electrodes and the upward shift of the quantum capacitance of N-doped monolayer graphene suggests that the interfacial capacitance of N-doped aMEGO electrodes does have a quantum component. N doping changes the electronic structure of the graphene, increasing the charge carrier density and thus modifying the quantum capacitance, and leads to larger values of interfacial capacitance. Understanding the relationship between the quantum capacitance and the interfacial capacitance of carbon electrodes is fundamentally important, and also relevant if further increases in capacitance are to be made. A quantum capacitance model quantitatively describing the change of the DOS by the dopants will lead to a better understanding of to what extent the quantum capacitance (if present as a limiting factor) affects the interfacial or electrode capacitance. This may lead to optimal design of the carbon electrodes (including their doping), and then to the optimal design of the overall ultra-capacitor cells to yield high values of specific capacitance and stored electrical energy.

Acknowledgements

We appreciate funding support from the U.S. Department of Energy (DOE) under award DE-SC0001951.

References

1 B. E. Conway, *Electrochemical Supercapacitors: Scientific Fundamentals and Technological Applications*, Kluwer Academic/Plenum Publisher, New York, 1999.
2 L. L. Zhang and X. S. Zhao, *Chem. Soc. Rev.*, 2009, **38**, 2520–2531.
3 M. F. El-Kady, V. Strong, S. Dubin and R. B. Kaner, *Science*, 2012, **335**, 1326–1330.
4 M. D. Stoller, S. Park, Z. Yanwu, J. An and R. S. Ruoff, *Nano Lett.*, 2008, **8**, 3498–3502.
5 Y. Zhu, S. Murali, M. D. Stoller, K. J. Ganesh, W. Cai, P. J. Ferreira, A. Pirkle, R. M. Wallace, K. A. Cychosz, M. Thommes, D. Su, E. A. Stach and R. S. Ruoff, *Science*, 2011, **332**, 1537–1541.

6 M. D. Stoller, C. W. Magnuson, Y. Zhu, S. Murali, J. W. Suk, R. Piner and R. S. Ruoff, *Energy Environ. Sci.*, 2011, **4**, 4685–4689.
7 C. Largeot, C. Portet, J. Chmiola, P. L. Taberna, Y. Gogotsi and P. Simon, *J. Am. Chem. Soc.*, 2008, **130**, 2730–2731.
8 H. M. Jeong, J. W. Lee, W. H. Shin, Y. J. Choi, H. J. Shin, J. K. Kang and J. W. Choi, *Nano Lett.*, 2011, **11**, 2472–2477.
9 W. Kim, J. B. Joo, N. Kim, S. Oh, P. Kim and J. Yi, *Carbon*, 2009, **47**, 1407–1411.
10 W. Li, D. Chen, Z. Li, Y. Shi, Y. Wan, G. Wang, Z. Jiang and D. Zhao, *Carbon*, 2007, **45**, 1757–1763.
11 M. Seredych, D. Hulicova-Jurcakova, G. Q. Lu and T. J. Bandosz, *Carbon*, 2008, **46**, 1475–1488.
12 F. Su, C. K. Poh, J. S. Chen, G. Xu, D. Wang, Q. Li, J. Lin and X. W. Lou, *Energy Environ. Sci.*, 2011, **4**, 717–724.
13 L. Zhao, L.-Z. Fan, M.-Q. Zhou, H. Guan, S. Qiao, M. Antonietti and M.-M. Titirici, *Adv. Mater.*, 2010, **22**, 5202–5206.
14 G. Lota and E. Frackowiak, *Fuel Cells*, 2010, **10**, 848–855.
15 Y. Qiu, X. Zhang and S. Yang, *Phys. Chem. Chem. Phys.*, 2011, **13**, 12554–12558.
16 J. P. Paraknowitsch, J. Zhang, D. Su, A. Thomas and M. Antonietti, *Adv. Mater.*, 2010, **22**, 87–92.
17 D. Hulicova-Jurcakova, M. Kodama, S. Shiraishi, H. Hatori, Z. H. Zhu and G. Q. Lu, *Adv. Funct. Mater.*, 2009, **19**, 1800–1809.
18 J. Xia, F. Chen, J. Li and N. Tao, *Nat. Nanotechnol.*, 2009, **4**, 505–509.
19 P. R. S. Dröscher, F. Molitor, P. Studerus, C. Stampfer, K. Ensslin and T. Ihn, *Appl. Phys. Lett.*, 2010, **96**, 152104–152106.
20 T. Fang, A. Konar, H. Xing and D. Jena, *Appl. Phys. Lett.*, 2007, **91**, 092109.
21 D. L. John, L. C. Castro and D. L. Pulfrey, *J. Appl. Phys.*, 2004, **96**, 5180–5184.
22 J. Casanovas, J. M. Ricart, J. Rubio, F. Illas and J. M. Jiménez-Mateos, *J. Am. Chem. Soc.*, 1996, **118**, 8071–8076.
23 X. Li, W. Cai, J. An, S. Kim, J. Nah, D. Yang, R. Piner, A. Velamakanni, I. Jung, E. Tutuc, S. K. Banerjee, L. Colombo and R. S. Ruoff, *Science*, 2009, **324**, 1312–1314.
24 Z. Jin, J. Yao, C. Kittrell and J. M. Tour, *ACS Nano*, 2011, **5**, 4112–4117.
25 A. C. Ferrari, J. C. Meyer, V. Scardaci, C. Casiraghi, M. Lazzeri, F. Mauri, S. Piscanec, D. Jiang, K. S. Novoselov, S. Roth and A. K. Geim, *Phys. Rev. Lett.*, 2006, **97**, 187401.
26 C. Casiraghi, S. Pisana, K. S. Novoselov, A. K. Geim and A. C. Ferrari, *Appl. Phys. Lett.*, 2007, **91**, 233108.
27 C. Stampfer, F. Molitor, D. Graf, K. Ensslin, A. Jungen, C. Hierold and L. Wirtz, *Appl. Phys. Lett.*, 2007, **91**, 241907.
28 C. Thomsen and S. Reich, *Phys. Rev. Lett.*, 2000, **85**, 5214–5217.
29 A. Das, S. Pisana, B. Chakraborty, S. Piscanec, S. K. Saha, U. V. Waghmare, K. S. Novoselov, H. R. Krishnamurthy, A. K. Geim, A. C. Ferrari and A. K. Sood, *Nat. Nanotechnol.*, 2008, **3**, 210–215.
30 X. Cao, Y. Shi, W. Shi, G. Lu, X. Huang, Q. Yan, Q. Zhang and H. Zhang, *Small*, 2011, **7**, 3163–3168.
31 L. Zhao, R. He, K. T. Rim, T. Schiros, K. S. Kim, H. Zhou, C. Gutiérrez, S. P. Chockalingam, C. J. Arguello, L. Pálová, D. Nordlund, M. S. Hybertsen, D. R. Reichman, T. F. Heinz, P. Kim, A. Pinczuk, G. W. Flynn and A. N. Pasupathy, *Science*, 2011, **333**, 999–1003.
32 T. Fang, A. Konar, H. Xing and D. Jena, *Appl. Phys. Lett.*, 2007, **91**, 092109.
33 J. H. Chen, C. Jang, S. Adam, M. S. Fuhrer, E. D. Williams and M. Ishigami, *Nat. Phys.*, 2008, **4**, 377–381.
34 S. Kasamatsu, S. Watanabe and S. Han, *Phys. Rev. B: Condens. Matter Mater. Phys.*, 2011, **84**, 085120.
35 E. H. Hwang, S. Adam and S. Das Sarma, *Phys. Rev. Lett.*, 2007, **98**, 186806.
36 J. Martin, N. Akerman, G. Ulbricht, T. Lohmann, J. H. Smet, K. von Klitzing and A. Yacoby, *Nat. Phys.*, 2008, **4**, 144–148.
37 Y. Zhang, V. W. Brar, C. Girit, A. Zettl and M. F. Crommie, *Nat. Phys.*, 2009, **5**, 722–726.
38 H. Xu, Z. Zhang and L.-M. Peng, *Appl. Phys. Lett.*, 2011, **98**, 133122–133123.
39 A. H. Castro Neto, F. Guinea, N. M. R. Peres, K. S. Novoselov and A. K. Geim, *Rev. Mod. Phys.*, 2009, **81**, 109–162.